Nanoconfined Iron Oxychloride Material as a High-Performance Cathode for Rechargeable Chloride Ion Batteries

Tingting Yu,[†] Qiang Li,[‡] Xiangyu Zhao,*,[†,∥] Hui Xia,[§] Liqun Ma,[†] Jinlan Wang,[‡] Ying Shirley Meng,*,[¶] and Xiaodong Shen[†,⊥]

[†]College of Materials Science and Engineering, Nanjing Tech University, 5 Xinmofan Road, Nanjing 210009, China

[∥]Jiangsu Collaborative Innovation Center for Advanced Inorganic Functional Composites, Nanjing Tech University, 5 Xinmofan Road, Nanjing 210009, China

[‡]School of Physics, Southeast University, Nanjing 211189, China

[§]School of Materials Science and Engineering, Nanjing University of Science and Technology, Xiaolingwei 200, Nanjing 210094, China

[¶]Department of NanoEngineering, University of California San Diego, La Jolla, California 92093, United States

[⊥]State Key Laboratory of Materials-Oriented Chemical Engineering, Nanjing Tech University, 5 Xinmofan Road, Nanjing 210009, China

S Supporting Information

ABSTRACT: As a group of attractive photoelectromagnetic and catalytic functional materials, metal oxychlorides have been attracting attention for electrochemical energy storage in rechargeable chloride ion battery (CIB) systems recently. Their application, however, is limited by the complicated synthesis and/or poor cycling stability. Herein, a facile strategy using vacuum impregnation and subsequent thermal decomposition at mild conditions has been developed to synthesize the FeOCl/CMK-3 nanocomposite material. Benefiting from the nanoconfined structure, a high-performance FeOCl/CMK-3 cathode, which has a high discharge capacity of 202 mAh g^{-1}, superior cycling stability, and significantly improved charge transfer and chloride ion diffusion, is achieved. The electrolyte component is found to show a high affinity with the chlorine layer in the FeOCl phase, inducing evident expansion of the FeOCl layers along the b-axis direction and thus boosting a new potential liquid exfoliation approach for preparing 2D FeOCl material. Importantly, reversible electrochemical reactions of the FeOCl cathode material based on the redox reactions of iron species and chloride ion transfer are revealed.
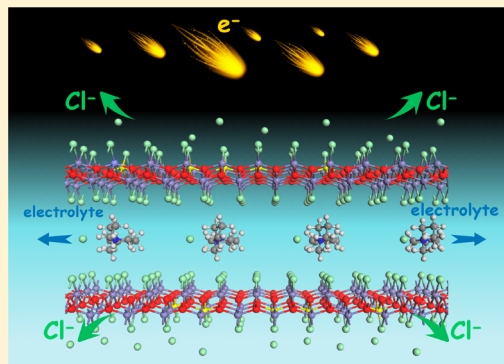
Metal oxychlorides MO$_x$Cl$_y$ (M = transition or rare earth metal) are a group of chemical compounds in which both oxygen and chlorine atoms are bonded to a metal element. They have strong in-plane M−O chemical bonds and weak out-of-plane van der Waals interaction between adjacent Cl−Cl layers.[1,2] This structure could facilitate the separation and transport of charge carriers,[3,4] contributing to the development of metal oxychlorides as high-efficiency photocatalysts for water splitting, environment remediation, and hydrogen production under UV or visible light.[4−6] The electronic, magnetic, and photoluminescent behaviors of metal oxychlorides are also of great interest.[7−9] Furthermore, applications of metal oxychlorides in glucose and gas sensors and Fenton-like catalysts for degradation of organic contaminants were also developed.[10−13] Recently, owing to high

stability, desired high theoretical energy density, and chlorine resources, metal oxychlorides such as BiOCl, FeOCl, and VOCl have been employed as cathode materials for chloride ion batteries (CIBs), which is a new rechargeable battery based on chloride ion transfer, using Li or Mg as the anode material.[14−20]

Besides the high theoretical energy density, FeOCl material possesses abundant elemental components. Currently, the synthesis of FeOCl is commonly performed by a complicated chemical vapor transport method, which requires a high temperature of 643 K (370 °C) for several days, leads to the formation of a large particle size of FeOCl, and brings about
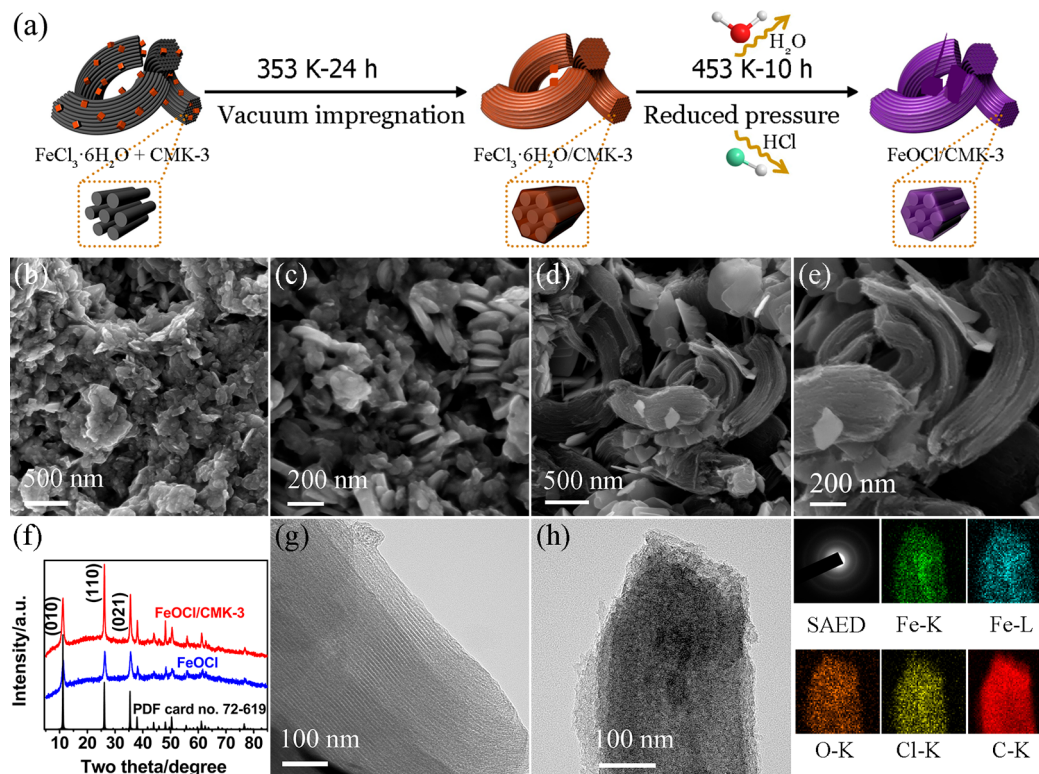
Figure 1. (a) Schematic fabrication process of the FeOCl/CMK-3 material. SEM images and XRD patterns of (b,c,f) the as-prepared FeOCl and (d,e,f) FeOCl/CMK-3 nanocomposite. (g) TEM image of the CMK-3 powder. (h) TEM image and the corresponding SAED and elemental mapping images of the FeOCl@CMK-3 nanocomposite.

high pressure during synthesis because of the vaporization of FeCl₃.[14,16,17] Therefore, a facile synthesis method of FeOCl is highly demanded. Second, FeOCl has a high electrical resistivity (ER) of 10^7 Ω·cm at ambient conditions,[21] which is 2 orders of magnitude higher than that of pure Si. Conventional carbon incorporation at high temperature for improving the electrical conductivity of FeOCl would not be realized because the decomposition of FeOCl occurs at around 643 K (370 °C).[22] Alternatively, mechanical milling of FeOCl with different carbon materials at room temperature was carried out, and the charge transfer resistance of the FeOCl cathode could be drastically decreased, resulting in an increase of the maximum discharge capacity.[17] Nevertheless, decomposition of FeOCl by mechanical milling was observed, as shown in Figure S1, and good cycling stability was not obtained. The third challenge for the application of FeOCl lies in buffering the large volume change during cycling. Theoretically, removal of the chlorines in FeOCl would cause a volume contraction of 58.6%. Actually, the issues concerning the high ER and large volume variation also exist in utilization of the attractive sulfur (ER: 10^{23} Ω·cm) or silicon electrode material in rechargeable batteries.[23,24] A nanoconfinement approach using porous carbon as the matrix enabled realization of high electronic conduction and structural integrity of these electrode materials during cycling.[24−27]

Herein, we report a nanoconfined FeOCl cathode material, which was successfully prepared by a thermal decomposition method and the incorporation of CMK-3 under mild conditions below 473 K. The as-prepared FeOCl/CMK-3 nanocomposite cathode shows a maximum discharge capacity of 202 mAh g^{-1} and a high reversible capacity of 162 mAh g^{-1} after 30 cycles, owing to the drastically enhanced charge

transfer and chloride ion diffusion. Intercalation of organic molecules and also the electrolyte into the layers of FeOCl before cycling has been observed. The electrochemical reaction mechanism based on chloride ion transfer of the FeOCl cathode material in CIBs is further elucidated.

A schematic fabrication process of the FeOCl/CMK-3 material is shown in Figure 1a. First, the FeCl₃·6H₂O and CMK-3 powders were mixed together in a mortar. The mixture was loaded into an evacuated and sealed quartz tube and then treated at 353 K for 24 h. Thereafter, the obtained FeCl₃·6H₂O/CMK-3 powders were heat treated at 453 K for 10 h in a flask under reduced pressure. The pure FeOCl material was prepared directly by this thermal decomposition method without the addition of CMK-3. Figure 1b−h shows the morphology and structure results of the as-prepared pure FeOCl and FeOCl/CMK-3 nanocomposites. The SEM images in Figure 1b,c represent an agglomerated morphology of the as-prepared FeOCl material. Some nanoflakes with a thickness of about 40 nm were also observed and aggregated in the bulk FeOCl particles. In contrast, the as-prepared FeOCl/CMK-3 nanocomposites exhibit distinct morphologies, including worm-like CMK-3 particles coexisting with some highly dispersed nanosheets with a thickness of about 20 nm (Figure 1d,e). This suggests that the addition of CMK-3 can prevent the agglomeration of FeOCl during its crystallization process by the thermal decomposition of FeCl₃·6H₂O. The corresponding XRD patterns in Figure 1f show that all of the reflections of both FeOCl and FeOCl/CMK-3 samples can be indexed and assigned to the orthorhombic layered FeOCl phase (PDF card no. 72-619) with three characteristic peaks corresponding to (010), (110), and (021) lattice planes. The decrease in the intensity ratio between (010) and (110) lattice planes indicates
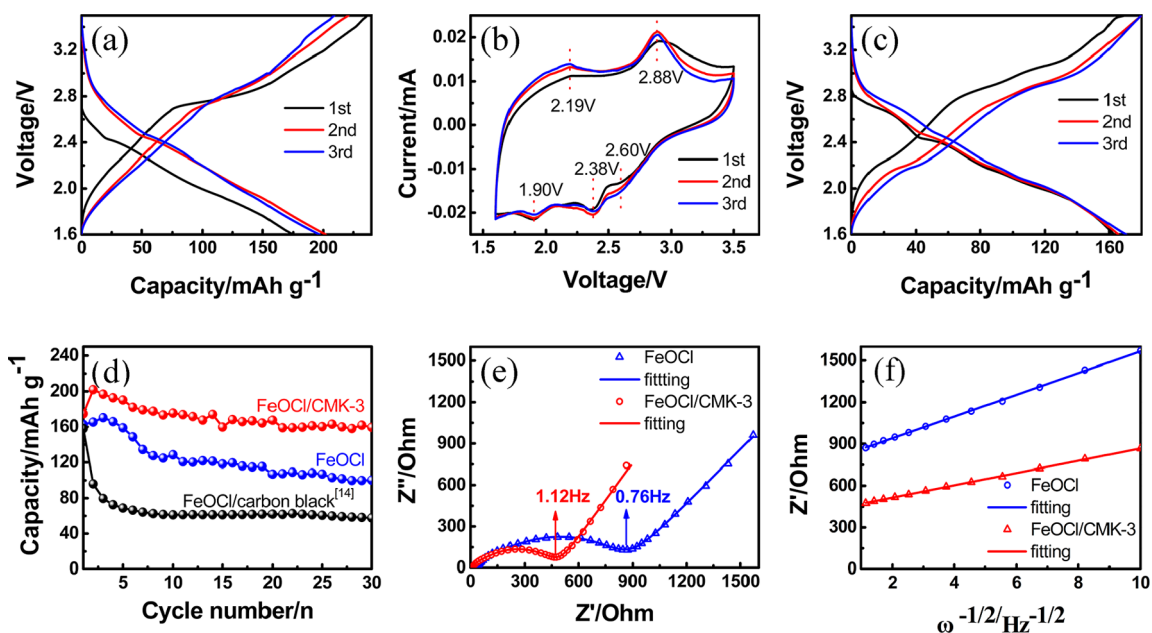
Figure 2. Discharge and charge curves (10 mA g^{-1}) and CV patterns (60 μV s^{-1}) of the as-prepared (a,b,d) FeOCl/CMK-3 and (c,d) FeOCl cathodes. (e) Nyquist plots and (f) the relationship between Z′ and $\omega^{-1/2}$ in the low-frequency region of the as-prepared FeOCl/CMK-3 and FeOCl cathodes.

the formation of thinner FeOCl layers in the FeOCl/CMK-3 sample. This is consistent with the SEM results in Figure 1d,e. TEM analysis was investigated to further illustrate the structure and morphology of CMK-3 and the FeOCl/CMK-3 nano-composite. CMK-3 shows its clear mesoporous channels with a pore size of about 4 nm in Figure 1g. After FeOCl loading, the apparent morphology of CMK-3 was retained, while the internal mesoporous channels were blocked, as shown in Figure 1h. The elemental mapping analysis of this sample reveals the uniform distribution of Fe, O, and Cl elements, and the corresponding EDS pattern in Figure S2 demonstrates the fine composition of the FeOCl in CMK-3, indicating the successful nanoconfinement of FeOCl in CMK-3 (FeOCl@CMK-3 nanohybrid) by vacuum impregnation and subsequent thermal decomposition. The corresponding selected area electron diffraction (SAED) image shows only the reflections of the semigraphitized CMK-3. This is consistent with the result of few-layer FeOCl nanosheets, which also showed no evident diffraction.[28]

Figure 2 shows the electrochemical properties of the FeOCl/Li electrode systems. The typical discharge and charge profiles of the electrode system using the as-prepared FeOCl/CMK-3 cathode are presented in Figure 2a. The FeOCl/CMK-3 cathode shows a discharge capacity of 174 mAh g^{-1} and a dominant two-step discharge stage at the first cycle. A maximum discharge capacity of 202 mAh g^{-1} (81% of the theoretical discharge capacity) was received after electro-chemical activation in the first cycle, which could be attributed to refinement of the particle/grain size by the conversion reaction.[14] The voltage hysteresis between discharge and charge was narrowed by this activation. The CV patterns of this electrode system in Figure 2b exhibit two dominant pairs of cathodic and anodic stages under the potential window of 1.6−3.5 V. The first reduction stage appears from 2.8 to 2.1 V and consists of a weak peak at 2.6 V and a distinct peak at 2.38 V. The corresponding oxidation stage is centralized at around 2.88 V. Another redox couple at the lower potential includes a

reduction peak at 1.9 V and the corresponding oxidation peak at 2.19 V. The increase in the peak current and the decrease in the potential gap after the first cycle are in accordance with the aforementioned activation process. Similar discharge and charge profiles (Figure 2c) were observed when the as-prepared FeOCl was used as the cathode. The pure FeOCl cathode has a maximum discharge capacity of 165 mAh g^{-1}, which is much lower than that of the as-prepared FeOCl/CMK-3 cathode. Upon cycling, an obvious capacity decay occurred and only 100 mAh g^{-1} (60.6% capacity retention rate) of the as-prepared FeOCl cathode was maintained after 30 cycles (Figure 2d). Still, this capacity is much higher than 60 mAh g^{-1} (37.5% capacity retention rate) of the FeOCl material fabricated by the chemical vapor transport method at high temperature, followed by mechanical milling with carbon black.[14] Therefore, the thermal decomposition of FeCl$_3$·6H$_2$O at mild conditions facilitates the formation of high-performance FeOCl material. In comparison with pure FeOCl, the as-prepared FeOC/CMK-3 cathode retained a high discharge capacity of 162 mAh g^{-1} (80.2% capacity retention rate) after 30 cycles. This indicates that the incorporation of CMK-3 in the FeOCl cathode contributes to significant improvements in the electrochemical activity and the structural stability of FeOCl, stimulating the addition of more CMK-3 in the FeOCl cathode. As shown in Figure S3, the diffraction peaks of the FeOCl were broaden and weakened by the increase in the CMK-3 content. This may be related to the decrease of FeOCl content and/or refinement in the particle/grain size of FeOCl. However, Fe$_2$O$_3$ was formed and chlorine content was decreased (Figure S3, EDS) when more CMK-3 was added, which may be caused by the delay in the release of water vapor during the decomposition of FeCl$_3$·6H$_2$O. The water vapor then reacted with the fresh FeOCl and led to the formation of Fe$_2$O$_3$, resulting in reduction of the active material content. As a consequence, the discharge capacity of the FeOCl cathode was evidently decreased when more CMK-3 was introduced, as shown in Figure S4.
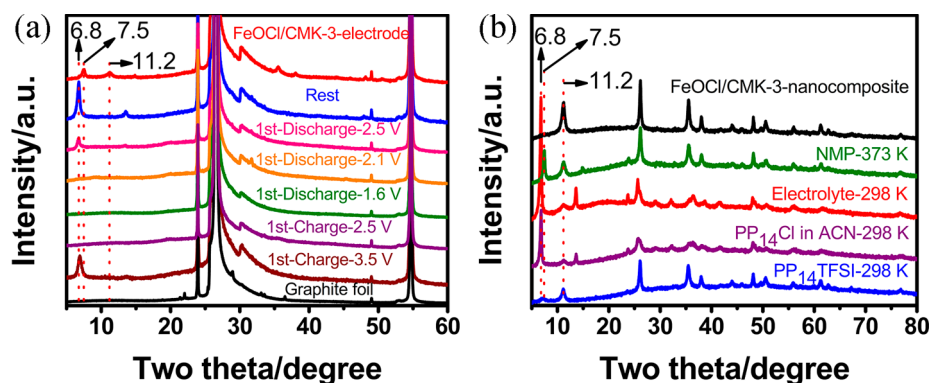
Figure 3. (a) XRD patterns of the FeOCl/CMK-3 electrodes at different charge and discharge states in the first cycle. (b) XRD patterns of the as-prepared FeOCl/CMK-3 powders and the powders treated by NMP at 373 K, electrolyte, PP$_{14}$TFSI, or PP$_{14}$Cl/ACN at 298 K for 10 h.

To understand the reasons for the impressive charge and discharge performance of the FeOCl/CMK-3 nanocomposite, electrochemical impedance spectroscopy (EIS) measurement was carried out (Figure 2e,f). The electrochemical processes of both the as-prepared FeOCl and FeOCl/CMK-3 electrode systems show a controlling step of a mixed rate-determining process containing charge transfer and chloride ion diffusion steps. The EIS curves consist of three parts, a semicircle at high frequency followed by a further semicircle and a straight line at low frequency (Figure 2e). The former semicircle extended to the Z' axis is reflected by a solution resistance (R_s), which includes ionic resistance from the separator and electrolyte. The former semicircle is considered to be the contact resistance (R_c), the later semicircle may be related to the charge transfer process (R_{ct}), and the straight line should be associated with the Warburg impedance by chloride ion diffusion.[17] The as-prepared FeOCl cathode shows a notable R_c of 161.6 Ohm and an R_{ct} of 573.9 Ohm. These values of the as-prepared FeOCl/CMK-3 nanocomposite were significantly decreased to 69.1 and 345.2 Ohm, implying that higher electrical conductivity and a faster charge transfer reaction were obtained for the as-prepared FeOCl/CMK-3 nanocomposite. From the straight line in the low-frequency range, the diffusion coefficient of the chloride ion is estimated according to the following equation[29]

$$D = (R^2 T^2)/(2 A^2 n^4 F^4 C^2 \sigma^2) \tag{1}$$

where D is the ionic diffusion coefficient, R is the gas constant, T is the absolute temperature, A is the surface area of the electrode, n is the number of electrons per molecule, F is the Faraday constant, C is the ionic concentration, and σ is the Warburg factor, which has a relationship with Z'

$$Z' \propto \sigma\omega^{-1/2} \tag{2}$$

Figure 2f represents the linear fittings of Z' vs the square root of the frequency ($\omega^{-1/2}$) in the low-frequency region. An evident lower slope of σ was observed for the FeOCl/CMK-3 cathode as compared with that of the FeOCl cathode, indicating that the FeOCl/CMK-3 cathode possessed enhanced chloride ion diffusion ability.[30]

To further understand the reaction mechanism of the FeOCl cathodes, ex situ XRD analysis (Figures 3 and S5) was performed to investigate the structural evolution of the FeOCl/CMK-3 and pure FeOCl electrodes at different electrochemical states. The diffraction peak at $2\theta = 26.5°$ is ascribed to reflection of the graphite foil current collector. Note that a new

diffraction peak at about 7.5° was formed after the slurry coating and subsequent drying of the FeOCl electrodes. Surprisingly, the main diffraction peak at 11.2° corresponding to the reflection of the (010) lattice plane of the FeOCl phase disappeared, and instead, another new strong peak at 6.8° appeared after a 10 h rest of the FeOCl electrodes in the coin cells. This means that the FeOCl interplanar spacing along the b-axis was significantly expanded before the charge and discharge testing. The diffraction peak of both FeOCl electrodes at 6.8° was weakened during discharge and disappeared after full discharge to 1.6 V. The following charge to 3.5 V of the FeOCl electrodes realized the recovery of this diffraction peak, accompanied by apparent peak broadening, which could be ascribed to refinement of the FeOCl grains. The reappearance of the diffraction peak at 6.8° after the recharge process indicates the formation of the expanded FeOCl and also the reversible reactions in the CIB. For the FeOCl/CMK-3 electrode, XRD characterization of the sample at intermediate discharge and charge states was also performed (Figure 3a). Upon discharge to 2.5 V, according to the discharge capacity in Figure 2a, the reaction with about 0.21 electron transfer occurred, and the reflections related to the FeOCl phase in the XRD pattern were notably decreased. When further discharged to 2.1 V, 0.56 electron was received at the FeOCl/CMK-3 electrode side and the reflections of the FeOCl phase almost disappeared. This may be caused by the structural collapse of the FeOCl phase after removal of more than 50% chloride ion according to the DFT calculations.[17] No reflections were observed after discharge to 1.6 V, indicating that amorphous and/or nano iron oxide particles were formed after the complete removal of chloride ion. After the following recharge to 3.5 V, the FeOCl reflections were recovered. This demonstrated that the FeOCl phase has better crystallinity than its corresponding iron oxide in a CIB during cycling.

In order to get an insight into the aforementioned lattice expansion of the FeOCl/CMK-3 electrode before cycling, the interaction between the FeOCl powders and NMP, the electrolyte or acetonitrile (ACN), which was used to wash the FeOCl electrodes after cycling, was investigated. Density functional theory (DFT) calculations were first performed on the adsorption energies on the FeOCl(010) surface of intercalation species, including NMP, PP$_{14}$Cl, and ACN, which was used by Zhang et al. to successfully exfoliate bulk FeOCl to 2D nanosheets.[28] The adsorption energies (Figure S6) follow the order of PP$_{14}$Cl > NMP > ACN and are −0.58, −0.45, and −0.20 eV, respectively. Compared with the cleave
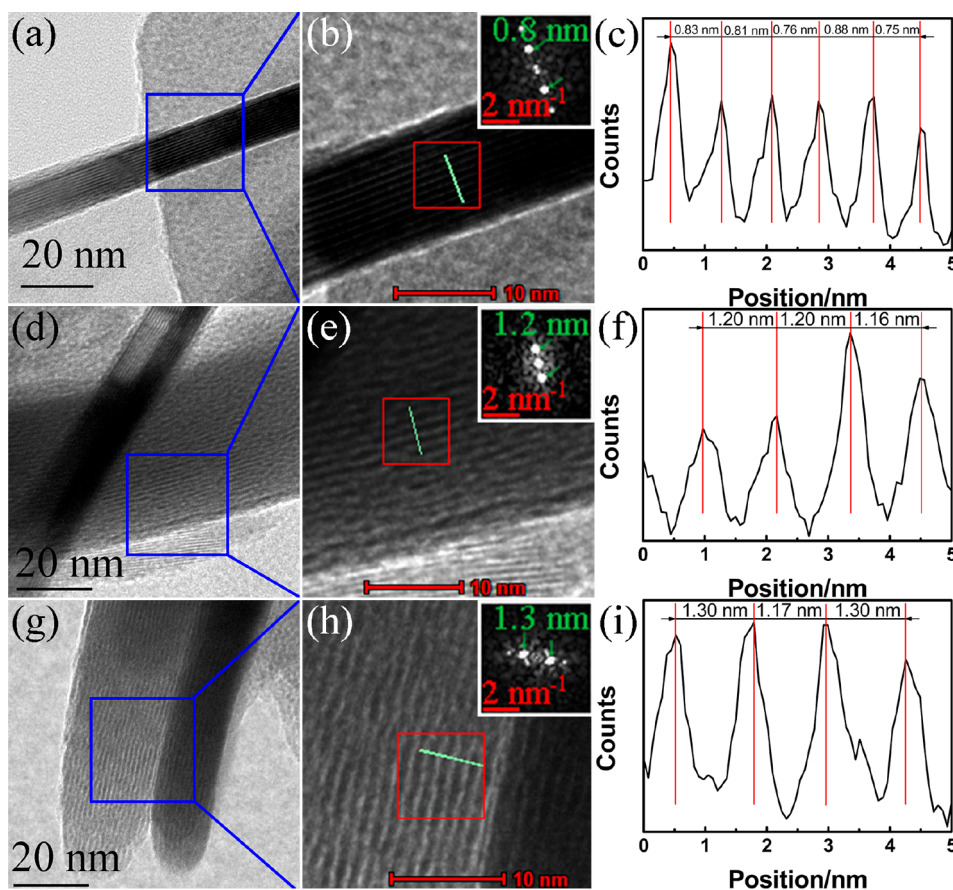
Figure 4. HRTEM images and the corresponding line profiles of (a−c) the FeOCl nanosheet in the as-prepared FeOCl/CMK-3 nanocomposite, (d−f) after electrode preparation, and (g−i) after soaking in the electrolyte for 10 h. The insets of panels (b,e,h) are the FFT patterns derived from the corresponding areas of the red squares.

energy (−0.1 eV, energy difference between interlayers) of FeOCl, all three species suggest energetically favorable driving forces for intercalation, and $PP_{14}Cl$ favors the most due to the strong intercalation between the charged piperidine ring and the lone pair of the surface chloride of FeOCl. For the intercalated FeOCl, the spacing between interlayers is clearly enlarged, depending on the size and organization of the molecules. For example, ACN and NMP show the same extension to 1.17 nm due to the methyl groups, while $PP_{14}Cl$ extends the interlayers to 1.33 nm. The corresponding intercalation experiments are conducted in the following. We immersed the FeOCl/CMK-3 powders into the NMP and found that NMP can be intercalated into the FeOCl layers after drying of the FeOCl/CMK-3 powders at 373 K, which leads to the increase of the FeOCl layer spacing from 0.79 (11.2°) to 1.20 (7.5°) nm (Figures 3b and 4d−f). This intercalation can also occur at the low temperature of 298 K (Figure S7), although it is weakened. The immersion of the as-prepared FeOCl/CMK-3 powders into the electrolyte results in a severe intercalation reaction only at the low temperature of 298 K by the formation of an intense diffraction peak at the lower position of 6.8°, indicating that the intercalation of the electrolyte component into the FeOCl layers occurred much easier and brought about a larger expansion of the FeOCl layers to 1.30 nm (Figure 4g−i). These expansion results are consistent with those obtained from the DFT calculations. We further verified that the main expansion from the intercalation of the electrolyte was contributed by the $PP_{14}Cl$,

as confirmed by the XRD results of the FeOCl/CMK-3 powders treated by the 0.5 M $PP_{14}Cl$ in ACN and $PP_{14}TFSI$ solution separately (Figure 3b). Therefore, both theoretical calculations and experiments reveal that NMP or $PP_{14}Cl$ (easier than ACN, Figure S7) can be intercalated into the FeOCl layers, resulting in an evident shift of the diffraction peak to the lower position of the FeOCl/CMK-3 and FeOCl electrode before cycling in Figures 3a and S5, rather than a self-discharge when the FeOCl/CMK-3 electrode is assembled into a coin cell. Furthermore, the intercalations can lead to distortion of lattices, as clearly shown by the TEM, HRTEM, and corresponding fast Fourier transform (FFT) patterns and line scan profiles of the as-prepared FeOCl nanosheets before and after intercalation (Figure 4). In this respect, our findings clarify the intercalation chemistry of the FeOCl electrode in the CIB system and may also boost the liquid exfoliation of FeOCl materials, contributing to the development and application of this new kind of 2D materials.

Figure 5 shows the structure and morphology evolution of the FeOCl/CMK-3 nanocomposite before and after discharge and charge in the first cycle. The FeOCl nanosheets in the nanocomposite were chosen and investigated to obtain a distinct evolution. Upon discharge, the as-prepared FeOCl nanosheet lost its smooth surface, and an obvious rough surface with many nanoparticles was formed (Figure 5d), which possessed ultralow chlorine content (inset in Figure 5d) and could be indexed to cubic Fe_3O_4 (PDF card no. 2-1035) with an ultrafine particle/grain size of 2−3 nm, as confirmed by the
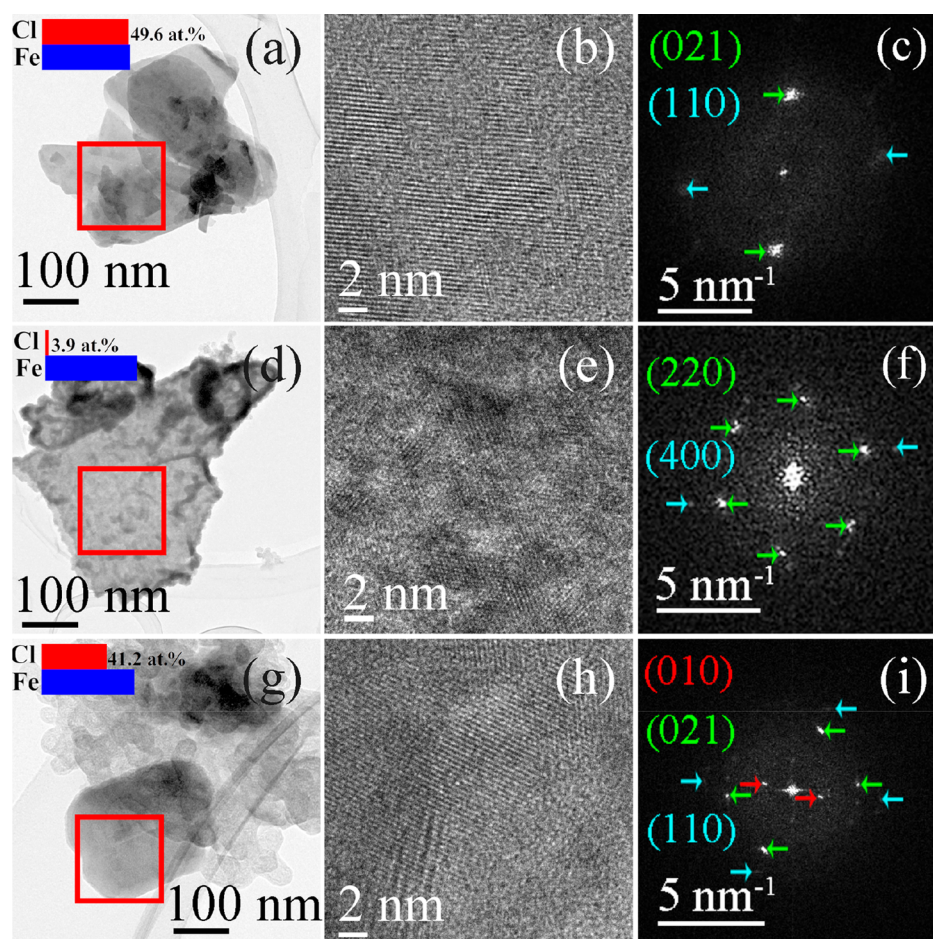
Figure 5. TEM images, HRTEM images, and the corresponding FFT patterns of the FeOCl nanosheets in the FeOCl/CMK-3 electrodes at different charge and discharge states in the first cycle: (a−c) as-prepared, (d−f) fully discharged, and (g−i) fully charged. The red squares in (a,d,g) correspond to the collected areas of EDS data. The obtained elemental contents of Cl and Fe by EDS are also inset in (a,d,g).
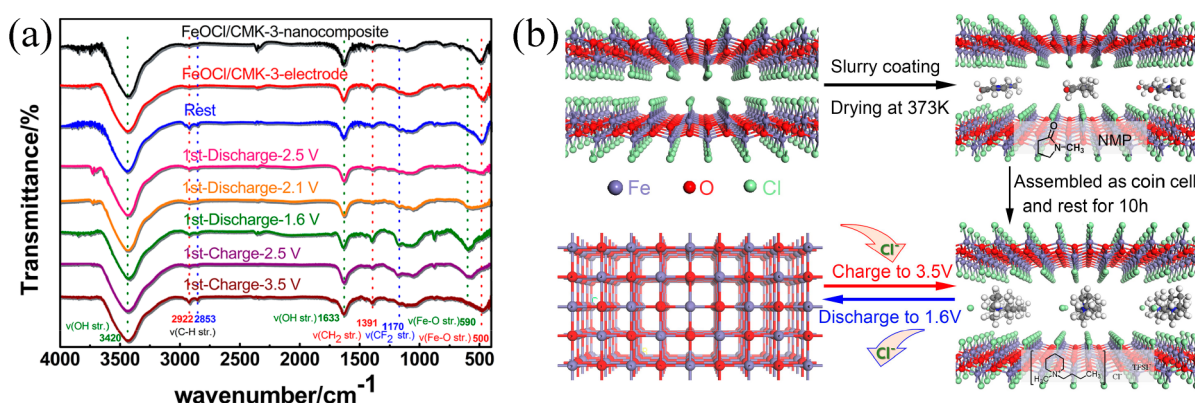

Figure 6. (a) FTIR spectra of the as-prepared FeOCl/CMK-3 powders, the as-prepared FeOCl/CMK-3 electrode, the FeOCl/CMK-3 electrode after rest in the coin cell (Rest), and the FeOCl/CMK-3 electrodes at discharge and charge at the first cycle. (b) Schematic illustration of the whole chemical and electrochemical processes of the FeOCl material before and after cycling.

HRTEM and the corresponding FFT results (Figure 5e,f). The formation of Fe_3O_4 could be attributed to the oxidation of FeO during the TEM test, which has an ultrafine size and is extremely sensitive. A similar result was reported in our previous work.[14] It is interesting that the smooth surface of the FeOCl phase was recovered after recharge (Figure 5g), and the corresponding EDS result (inset in Figure 5g and Figure S8) indicated that the chloride ion moved back to the cathode. The HRTEM and the corresponding FFT images (Figure 5h,i) of

the recharged FeOCl sample showed the formation of the FeOCl phase with a nanosize of 5−10 nm, which interpreted the refinement of the FeOCl grain size after cycling. These findings are consistent with the XRD result in Figure 3a that reversible electrochemical reaction of the as-prepared FeOCl electrode occurs via chloride ion transfer.

Fourier transform infrared spectroscopy (FTIR) measurement was performed to further analyze the phase transformation of the as-prepared FeOCl/CMK-3 samples before

and after cycling, as shown in Figure 6a. The regions around 1633 and 3420 cm^{-1} are related to the stretching vibrations of the hydroxyl group (−OH) in the adsorbed water during the FTIR test.[31] The bands of CH_2 symmetric and asymmetric stretching vibrations at 2853 and 2922 cm^{-1} were detected in all of the FeOCl electrodes;[32] however, the signals were very weak. The interaction between the as-prepared FeOCl powders and NMP or the electrolyte was also observed by FTIR (Figure S9). The results manifested that the NMP or the electrolyte was kept in the powders, although the signals were very weak. The intercalation chemistry of the FeOCl/CMK-3 samples before cycling, as shown in the XRD patterns (Figure 3), can also be confirmed by FTIR. The intercalation of NMP or the electrolyte does not change the Fe−O stretching at 500 cm^{-1} in the FeOCl phase,[33,34] while a weak signal related to Fe^{2+} (Fe−O) at 590 cm^{-1} was detected for the FeOCl/CMK-3 cathode after rest in the coin cell for 10 h.[35] This may be ascribed to partial self-discharge of the coin cell. Upon discharge, the Fe^{2+} signal increased and the Fe−O stretching of the FeOCl phase was weakened. For the FeOCl/CMK-3 electrode after the full discharge, the distinct band at 590 cm^{-1} was formed. This indicates the formation of Fe^{2+} after the dechlorination during discharge. The band at 500 cm^{-1} related to the FeOCl phase was recovered after recharge, although part of the phase with low iron valence still existed. The reversible electrochemical reaction based on the chloride ion transfer of the FeOCl/CMK-3 cathode in the CIB was further revealed. A schematic illustration in Figure 6b shows the whole chemical and electrochemical processes of the FeOCl material before and after cycling. NMP was intercalated into the FeOCl layers during preparation of the FeOCl cathode, inducing a large expansion of the FeOCl layers along the b-axis direction. Then, a further expansion was created by the intercalation of the electrolyte components when the FeOCl cathode was rested in the coin cell. The following process of the FeOCl cathode was the reversible electrochemical reaction upon chloride ion transfer during the discharge and charge cycling.

In summary, we developed a facile approach for preparing FeOCl with high performance for CIBs, and the reaction mechanisms of the FeOCl cathode material are unveiled accordingly. The FeOCl cathode material that was incorporated by CMK-3 under mild conditions shows a high discharge capacity of 202 mAh g^{-1} and superior cycling stability, which contributed to a distinct nanoconfined effect and significant enhancements in the charge transfer and chloride ion diffusion. XRD, TEM/HRTEM, EDS, and FTIR results revealed the Fe^{3+}/Fe^{2+} electrochemical reaction based on the chloride ion transfer of the FeOCl/CMK-3 electrode during cycling. Furthermore, chemical intercalations of NMP and the electrolyte components into the FeOCl layers, which induced evident expansion of the FeOCl layers along the b-axis direction, were clearly manifested. The electrolyte components showed a high affinity for the chlorine layer in the FeOCl phase. These findings bring a new potential liquid exfoliation approach for preparing 2D iron oxychloride material, boosting prospective applications of this new kind of 2D material in diverse areas of catalysis, degradation of organic contaminants, sensors, and electronics.

■ ASSOCIATED CONTENT

ⓢ Supporting Information

The Supporting Information is available free of charge on the ACS Publications website at DOI: 10.1021/acsenergy-lett.7b00699.

> Experimental section, photos of the acetone solutions with immersion of different FeOCl materials after 48 h, EDS pattern of the as-prepared FeOCl@CMK-3 powder, XRD and SEM/EDS patterns of the FeOCl/CMK-3 with different CMK-3 contents, cycling performance of the FeOCl/CMK-3 with different CMK-3 contents, XRD patterns of the as-prepared FeOCl electrode before and after cycling, DFT calculations, immersion test in NMP or ACN, EDS patterns of the FeOCl/CMK-3 electrodes before and after cycling, and FTIR spectra (PDF)

■ AUTHOR INFORMATION

Corresponding Authors
*E-mail: xiangyu.zhao@njtech.edu.cn (X.Z.).
*E-mail: shirleymeng@ucsd.edu (Y.S.M.).

ORCID ⓘ
Xiangyu Zhao: 0000-0002-9095-4494
Hui Xia: 0000-0002-2517-2410
Jinlan Wang: 0000-0002-4529-874X

Author Contributions
The manuscript was written through contributions of all authors. All authors have given approval to the final version of the manuscript.

Notes
The authors declare no competing financial interest.

■ ACKNOWLEDGMENTS

■ REFERENCES

(1) Nicolosi, V.; Chhowalla, M.; Kanatzidis, M. G.; Strano, M. S.; Coleman, J. N. Liquid Exfoliation of Layered Materials. *Science* **2013**, *340*, 1226419.

(2) Kargina, I.; Richeson, D. Diamine Intercalates of Titanium and Vanadium Oxychloride. Evidence for the Subsequent Substitution Reactions of TiOCl with Amines. *Chem. Mater.* **1996**, *8*, 480−485.

(3) Zhao, K.; Zhang, L. Z.; Wang, J. J.; Li, Q. X.; He, W. W.; Yin, J. J. Surface Structure-Dependent Molecular Oxygen Activation of BiOCl Single-Crystalline Nanosheets. *J. Am. Chem. Soc.* **2013**, *135*, 15750−15753.

(4) Mi, Y.; Wen, L. Y.; Wang, Z. J.; Cao, D. W.; Xu, R.; Fang, Y. G.; Zhou, Y. L.; Lei, Y. Fe(III) Modified BiOCl Ultrathin Nanosheet Towards High-efficient Visible-light Photocatalyst. *Nano Energy* **2016**, *30*, 109−117.

(5) Fujito, H.; Kunioku, H.; Kato, D.; Suzuki, H.; Higashi, M.; Kageyama, H.; Abe, R. Layered Perovskite Oxychloride Bi$_4$NbO$_8$Cl: A Stable Visible Light Responsive Photocatalyst for Water Splitting. *J. Am. Chem. Soc.* **2016**, *138*, 2082−2085.

(6) Tu, H.; Xu, L. L.; Mou, F. Z.; Guan, J. G. Single Crystalline Tantalum Oxychloride Microcubes: Controllable Synthesis, Formation Mechanism and Enhanced Photocatalytic Hydrogen Production Activity. *Chem. Commun.* **2015**, *51*, 12455−12458.

(7) Romero, F. D.; Coyle, L.; Hayward, M. A. Structure and Magnetism of Sr$_3$Co$_2$O$_4$Cl$_2$-An Electronically Driven Lattice Distortion in an Oxychloride Containing Square Planar Co-II Centers. *J. Am. Chem. Soc.* **2012**, *134*, 15946−15952.

(8) Myung, Y.; Wu, F.; Banerjee, S.; Stoica, A.; Zhong, H. X.; Lee, S. S.; Fortner, J.; Yang, L.; Banerjee, P. Highly Conducting, n-Type Bi$_{12}$O$_{15}$Cl$_6$ Nanosheets with Superlattice-like Structure. *Chem. Mater.* **2015**, *27*, 7710−7718.

(9) Li, X. H.; Deng, X.; Zhu, H.; Feng, J.; Peng, Y.; Bai, J. T.; Zheng, X. L.; Fan, H. B.; Wang, M. Z.; Chen, H. W. Well-Defined Flowerlike NdOCl Nanostructures: Nonaqueous Sol-Gel Synthesis, Nanoscale Characterization and Their Magnetic and Photoluminescence Properties. *Chem. - Asian J.* **2014**, *9* (2), 584−589.

(10) Gopalan, A. I.; Muthuchamy, N.; Lee, K. P. A Novel Bismuth Oxychloride-graphene Hybrid Nanosheets Based Non-enzymatic Photoelectrochemical Glucose Sensing Platform for High Performances. *Biosens. Bioelectron.* **2017**, *89*, 352−360.

(11) Dziubaniuk, M.; Trzesiec, M.; Pasierb, P.; Rekas, M. Application of Anion-conducting Lanthanum Oxychloride for Potentiometric Chlorine Gas Sensors. *Solid State Ionics* **2012**, *225*, 324−327.

(12) Wang, Y. Y.; Zhang, H. W.; Zhu, Y. D.; Dai, Z. F.; Bao, H. M.; Wei, Y.; Cai, W. P. Au-NP-Decorated Crystalline FeOCl Nanosheet: Facile Synthesis by Laser Ablation in Liquid and its Exclusive Gas Sensing Response to HCl at Room Temperature. *Adv. Mater. Interfaces* **2016**, *3* (9), 1500801.

(13) Yang, X. J.; Xu, X. M.; Xu, J.; Han, Y. F. Iron Oxychloride (FeOCl): An Efficient Fenton-Like Catalyst for Producing Hydroxyl Radicals in Degradation of Organic Contaminants. *J. Am. Chem. Soc.* **2013**, *135*, 16058−16061.

(14) Zhao, X. Y.; Zhao-Karger, Z.; Wang, D.; Fichtner, M. Metal Oxychlorides as Cathode Materials for Chloride Ion Batteries. *Angew. Chem., Int. Ed.* **2013**, *52*, 13621−13624.

(15) Gao, P.; Zhao, X. Y.; Zhao-Karger, Z.; Diemant, T.; Behm, R. J.; Fichtner, M. Vanadium Oxychloride/Magnesium Electrode Systems for Chloride Ion Batteries. *ACS Appl. Mater. Interfaces* **2014**, *6*, 22430−22435.

(16) Zhao, X. Y.; Li, Q.; Zhao-Karger, Z.; Gao, P.; Shen, X. D.; Fichtner, M.; Fink, K. Magnesium Anode for Chloride Ion Batteries. *ACS Appl. Mater. Interfaces* **2014**, *6*, 10997−11000.

(17) Zhao, X. Y.; Li, Q.; Yu, T. T.; Yang, M.; Fink, K.; Shen, X. D. Carbon Incorporation Effects and Reaction Mechanism of FeOCl Cathode Materials for Chloride Ion Batteries. *Sci. Rep.* **2016**, *6*, 19448.

(18) Gao, P.; Reddy, M. A.; Mu, X. K.; Diemant, T.; Zhang, L.; Zhao-Karger, Z.; Chakravadhanula, V. S. K.; Clemens, O.; Behm, R. J.; Fichtner, M. VOCl as a Cathode for Rechargeable Chloride Ion Batteries. *Angew. Chem., Int. Ed.* **2016**, *55*, 4285−4290.

(19) Zhao, X. Y.; Ren, S.; Bruns, M.; Fichtner, M. Chloride Ion Battery: A New Member in the Rechargeable Family. *J. Power Sources* **2014**, *245*, 706−711.

(20) Gschwind, F.; Euchner, H.; Rodriguez-Garcia, G. Chloride Ion Battery Review: Theoretical Calculations, State of the Art, Safety, Toxicity, and an Outlook towards Future Developments. *Eur. J. Inorg. Chem.* **2017**, *2017*, 2784−2799.

(21) Kim, S. H.; Kang, J. K.; Hwang, S. G.; Kim, H. J. A Theoretical-Study on the Electronic-Structures of Mocl (M = Ti, V and Fe) and Their Relationship with Physical-Properties. *Bull. Korean Chem. Soc.* **1995**, *16*, 299−304.

(22) Dai, Y. D.; Yu, Z.; Huang, H. B.; He, Y.; Shao, T.; Hsia, Y. F. Thermal Decomposition of Iron Oxychloride as Studied by Thermal Analysis, X-ray Diffraction and Mossbauer Spectroscopy. *Mater. Chem. Phys.* **2003**, *79*, 94−97.

(23) Zuo, X. X.; Zhu, J.; Muller-Buschbaum, P.; Cheng, Y. J. Silicon Based Lithium-ion Battery Anodes: A Chronicle Perspective Review. *Nano Energy* **2017**, *31*, 113−143.

(24) Zhang, J.; Yang, C. P.; Yin, Y. X.; Wan, L. J.; Guo, Y. G. Sulfur Encapsulated in Graphitic Carbon Nanocages for High-Rate and Long-Cycle Lithium-Sulfur Batteries. *Adv. Mater.* **2016**, *28*, 9539−9544.

(25) Yang, J. P.; Wang, Y. X.; Chou, S. L.; Zhang, R. Y.; Xu, Y. F.; Fan, J. W.; Zhang, W. X.; Kun Liu, H.; Zhao, D. Y.; Xue Dou, S. Yolk-shell Silicon-mesoporous Carbon Anode with Compact Solid Electrolyte Interphase Film for Superior Lithium-ion Batteries. *Nano Energy* **2015**, *18*, 133−142.

(26) Agyeman, D. A.; Song, K.; Lee, G. H.; Park, M.; Kang, Y. M. Carbon-Coated Si Nanoparticles Anchored between Reduced Graphene Oxides as an Extremely Reversible Anode Material for High Energy-Density Li-Ion Battery. *Adv. Energy Mater.* **2016**, *6*, 1600904.

(27) Wang, Y. X.; Yang, J. P.; Lai, W. H.; Chou, S. L.; Gu, Q. F.; Liu, H. K.; Zhao, D. Y.; Dou, S. X. Achieving High-Performance Room-Temperature Sodium Sulfur Batteries With S@Interconnected Mesoporous Carbon Hollow Nanospheres. *J. Am. Chem. Soc.* **2016**, *138*, 16576−16579.

(28) Zhang, J.; Jiao, X. L.; Xia, Y. G.; Liu, F. F.; Pang, Y. P.; Zhao, X. F.; Chen, D. R. Enhanced Catalytic Activity in Liquid-Exfoliated FeOCl Nanosheets as a Fenton-Like Catalyst. *Chem. - Eur. J.* **2016**, *22*, 9321−9329.

(29) Yang, M.; Zhao, X.; Bian, Y.; Ma, L.; Ding, Y.; Shen, X. Cation Disordered Rock Salt Phase Li$_2$CoTiO$_4$ as a Potential Cathode Material for Li-ion Batteries. *J. Mater. Chem.* **2012**, *22*, 6200−6205.

(30) Wang, S.; Zhang, Z.; Jiang, Z.; Deb, A.; Yang, L.; Hirano, S.-i. Mesoporous Li$_3$V$_2$(PO4)$_3$@CMK-3 Nanocomposite Cathode Material for Lithium Ion Batteries. *J. Power Sources* **2014**, *253*, 294−299.

(31) Xiao, F.; Li, W.; Fang, L.; Wang, D. Synthesis of Akageneite (beta-FeOOH)/Reduced Graphene Oxide Nanocomposites for Oxidative Decomposition of 2-chlorophenol by Fenton-Like Reaction. *J. Hazard. Mater.* **2016**, *308*, 11−20.

(32) Borodko, Y.; Habas, S. E.; Koebel, M.; Yang, P. D.; Frei, H.; Somorjai, G. A. Probing the Interaction of Poly(vinylpyrrolidone) with Platinum Nanocrystals by UV-Raman and FTIR. *J. Phys. Chem. B* **2006**, *110*, 23052−23059.

(33) Sakaebe, H.; Higuchi, S.; Kanamura, K.; Fujimoto, H.; Takehara, Z. Preparation of a FeOCl Derivative with Pyrrole and Its Performance as a Cathode Material in a Secondary Lithium Battery System. *J. Power Sources* **1995**, *56*, 165−169.

(34) Scully, S. F.; Bissessur, R.; Dahn, D. C.; Xie, G. H. In Situ Polymerization/Intercalation of Substituted Anilines into Iron (III) Oxychloride. *Solid State Ionics* **2010**, *181*, 933−938.

(35) Sitthichai, S.; Pilapong, C.; Thongtem, T.; Thongtem, S. CMC-coated Fe$_3$O$_4$ Nnanoparticles as New MRI Probes for hepatocellular carcinoma. *Appl. Surf. Sci.* **2015**, *356*, 972−977.